

Supporting Calculations for NASA's IRIS Mission. II. The C II 1335Å lines

Eugene Avrett and Sean McKillop

Harvard-Smithsonian Center for Astrophysics, 60 Garden Street, Cambridge, MA 02138

This is the second of a series of reports showing calculated solar line spectra for comparison with observations from NASA's IRIS spacecraft, to be launched in 2013. The first of these reports (posted at www.cfa.harvard.edu/~avrett) gave results for the Mg II k line at 2796.5 Å. The present report gives results for the C II multiplet with component lines centered at 1334.53, 1335.66, and 1335.71 Å.

The principal lines to be observed by IRIS are those of Mg II 2796.5, 2803.5 Å, O I 1335.6 Å, C II 1334.5, 1335.7 Å, O IV 1399.8, 1401.2 Å, and Si IV 1393.8, 1402.8 Å. These are all emission lines, formed mainly in the solar chromosphere. We calculate the profiles of these lines at various disk positions, and for various mass-conserving flow velocities, for three 1-dimensional atmospheric models corresponding to the faint and mean internetwork, and bright network, designated as models A, B, and F, respectively.

The three component models are those determined by Fontenla et al. (2011). Figure 1 shows the temperature as a function of height for these models which were derived to obtain approximate agreement between the calculated and observed intensities from the given regions over a wide range of wavelengths. We find that the available observations generally fall within the limits of the three models A, B, and F. The brighter component models are not considered since they give results beyond the range of the HRTS observations considered.

The chromosphere-corona transition regions in these models take account of ambipolar diffusion and energy balance, but the calculated intensities are in better agreement with observations than were obtained in the earlier papers that included these effects. Fontenla et al. show that the corresponding calculated full-disk irradiances, determined from the component intensities from the pattern of quiet and active regions as a function of time, are in reasonable agreement with the observed irradiances over the last solar cycle. Also, Linsky et al. (2012) found that these models roughly account for continuum emission in the far ultraviolet from the chromospheres of solar-mass stars. While these models are 1-dimensional and time-independent, they should nevertheless provide a useful first approximation for interpreting IRIS observation at high spatial and temporal resolution.

The website <http://www.digidyna.com/Results2010> lists the atmospheric parameters for the three Fontonla et al. models. We adopt their values for the temperature T and the total hydrogen density nH as functions of height in the atmosphere. They list other parameters as well, including the electron number density ne, but we redetermine ne from the calculated proton and other ion densities, assuming charge neutrality.

Given T and nH vs. height for each model, we solve the coupled equations of radiative transfer

and statistical equilibrium for the bound-bound and bound-free transitions of H, H⁻, He I-II, C I-IV, O I-VI, Na I-II, Mg I-II, Al I-II, Si I-IV, S I-IV, Ca I-II, and Fe I-II. For each of these 32 atoms and ions we compute the populations of the bound energy levels along with the degree of ionization from one stage to the next. These are non-LTE optically thick calculations which determine the number densities vs. height and the intensity of radiation vs. both height and frequency throughout the continuum and in each line. The continuum radiation, which affects all ionization calculations, is determined mainly by H, H⁻, He I-II, O I-III, Na I, Mg I, Al I, Si I, S I, Ca I, and Fe I. The higher ion populations must be calculated to determine the fractional elemental abundance vs. height in each ion stage, including the lowest. Given the results obtained with this set of atoms and ions we then calculate other line spectra such as from N I-IV and Ne I-VIII, along with detailed spectra throughout the three IRIS wavelength bands 1332-1358, 1390-1406, and 2784-2836 Å.

Thus, for a given temperature distribution, up to 100 separate multilevel calculations are needed to determine all the interactions between the atom and ion populations and to determine the line and continuum radiation throughout the atmosphere. This is feasible for the 1-dimensional time-dependent cases we consider, but accounting for all of these interactions may be impractical in current 3-dimensional time-dependent modeling, given that the spatial grid needed in 3-D is so much larger and that the full set of calculations must be carried out at each time step. These separate 1-D runs are made by hand, involving copying output files to a common input master file to account for degree of ionization of each constituent, but labor would be reduced by automating this process.

In the present 1-D calculations we do not solve the hydrostatic equilibrium equation, since we use the values of nH given by Fontenla et al. (2010). They calculate nH by a different method than the one used earlier by Fontenla, Avrett, & Loeser (1990, 1991, 1993, 2002), Avrett & Loeser (2008), Fontenla et al. (2006), and Vernazza, Avrett, & Loeser (1981). The height where the temperature abruptly increases to form the chromosphere-corona transition region is determined to be in the range 1700-2000 km above the photosphere according to He I line observations (see Avrett, Fontenla, & Loeser 1994). Model calculations assuming hydrostatic equilibrium with only gas pressure balancing solar gravity place the transition several hundred km lower, implying the need for additional pressure, or some outward force, to extend the chromosphere to agree with observations. The earlier method added turbulent pressure to the gas pressure, based on the non-thermal velocity distribution inferred from the observed Doppler widths of lines formed at various heights which exceed thermal Doppler widths. The new method of Fontenla et al. (2009, 2011) instead introduces a magnetic-related outward force distribution, determined empirically but consistent with observations, that not only extends the chromosphere but also lowers the minimum temperature values that occur between the photosphere and chromosphere to account for the infrared carbon monoxide lines. We do not compare the two methods here, but adopt the three new models as a set that has been calculated in the same way and represent the full range of brightness features on the solar disk, apart from sunspots and flares.

Our atomic model for C II consists of 15 bound levels, and the C III continuum. The model

includes 22 line transitions, all consisting of multiplets with 2 to 7 components. Here we discuss the C II multiplet with components at wavelengths 1334.53, 1335.66, and 1335.71 Å. These components have respective opacities 0.501, 0.050, and 0.449 times the total opacity for this combined transition. The blend of the two lines at 1335.66 and 1335.71 Å makes the combined line slightly wider.

A detailed discussion of the C II 1335 Å multiplet is given in Section 16.1 of Avrett & Loeser (2008). Figure 20 of that paper shows, for the 1334.53 component, the variation with height of: the Planck function, the line source function, the net radiative cooling rate, and the contributions functions dI/dh for the line center, the blue peak, and the blue wing of the line. The calculated line shown there has a central reversal, which disappears when instrumental broadening and averaging along the slit is taken into account. The line is calculated from an average quiet-Sun model, based on the SUMER atlas of Curdt et al (2001), and uses the "old" determination of nH that uses turbulent pressure. The profile shown in panel 33 of Figure 19 of that paper only roughly agrees with the profiles given in the present report for the internetwork and network models, indicating that the models still need adjustments to fit the observations.

Figure 2 shows the C II multiplet profiles at disk center for the three brightness-component models A, B, and F identified earlier.

Our calculated center-to-limb profiles for $\mu = 1., .7, .4, .2, .1,$ and $.05$ appear in Figures 3–5 for models A, B, and F respectively. Note that the profiles strongly brighten toward to limb.

Finally, for the three models, we give the calculated disk-center profiles for mass-conserving inflows in Figure 6-8, and outflows in Figure 9–11, of 10, 20, and 50 km/s. These velocities are the values at $nH = 10^{10} cm^{-3}$, and they vary with height as $1/nH$. The same inflow and outflow velocities were used in our first report for the Mg II k-line profiles.

For a general comparison, we show in Figure 12 the disk-center profiles of the C II lines for a sunspot SP, an average quiet region QS, and a coronal hole CH, obtained from the SUMER satellite by Curdt et al. (2001). We also show the three calculated profiles.

Figures 13 shows the profiles SP, QS, and CH again along with four profiles from the HRTS rocket flights, Brekke (1993). The HRTS profiles are identified as follows.

Feature	Abbreviation	Position
Quiet Sun	QR	$\mu=0.85-0.86$
Active region	AR	$\mu=0.85$
Sunspot A	SPA	$\mu=0.78$
Sunspot B	SPB	$\mu=0.76$

The values of μ on the solar disk where observations were taken are indicated.

Figure 14 shows seven profiles from regions of greater activity.

Feature	Abbreviation	Position
Quiet region A	QRA	$\mu=0.92-0.98$
Quiet region B	QRB	$\mu=0.65-0.70$
Quiet region L	QRL	$\mu=0.17-0.20$
Active region	ARL	$\mu=0.25-0.36$
Explosive event	EE	$\mu=0.62$
Light bridge	LB	$\mu=0.79$
Prominence	PR	—

A previous modeling study of these C II lines was carried out by Lites, Shine, & Chipman (1978) based on OSO 8 observations, using the quiet-Sun model of Vernazza et al. (1973), an early version of the subsequent model C of Vernazza et al. (1978). These models included an ad hoc temperature plateau of about 20,000 K in the transition region in order to account for the observed emission in the hydrogen Lyman lines. A transition region without such a plateau that has a temperature gradient steep enough to transport energy downward by thermal conduction to provide the energy emitted by the Lyman lines does not have sufficient optical thickness to account for the observed line emission. This problem was resolved by the introduction of ambipolar diffusion (see the four cited papers by Fontenla, Avrett, & Loeser) whereby ions from the upper transition region diffuse downward and recombine, releasing the energy needed for Lyman line emission. Also, neutrals diffuse upward into high-temperature regions. This diffusion of ions and atoms was treated by adding advection terms to the statistical equilibrium equations when the temperature gradient is so steep that ionized and neutral regions are in close proximity. Ambipolar diffusion should be taken into account whenever these conditions occur, in 3-D dynamical modeling as well as in 1-D modeling.

Current 1-D models of the transition region no longer have a temperature plateau. Lites et al. found that substantial C II line emission originated in the plateau region, so that some of their conclusions may need to be modified. The calculations carried out for the present report indicate that the C II 1335 A lines are formed in the upper chromosphere, with little influence from the transition region (see Figures 18 and 20 of Avrett & Loeser 2008). Wikstol, Hansteen, Carlsson, & Judge (2000), from an analysis of SUMER observations, found evidence for a transition-region contribution. They regarded the C II lines as being formed at a temperature of approximately 20,000 K, characteristic of the earlier plateau. Judge, Carlsson, & Stein (2003) also discussed this C II multiplet based on both 3-D and 1-D calculations. They also suggested that these lines are formed in the transition region; their 1-D results were based on model A of Vernazza et al. (1981) which included the transition-region plateau. Our results indicate that optical depth unity in these lines occurs near 1500 km where the temperature is near 6200 K.

While the present models only approximately fit the observations, we find that the lines are formed in a remarkably narrow range of temperatures, as shown in Figure 1. Even though the present 1-D models are not unique, we would consider it remarkable that dynamical models give similar results.

Note that the calculated profiles with flow velocities do not have the shape of the observed profiles. The observed profiles also have much larger Doppler widths than are calculated, indicating that the non-thermal velocity distributions in the models need to be increased. The brighter models P and Q of Fontenla et al. corresponding to bright plage and bright facula seem outside the range of the HRTS observations. These matters will be addressed in a subsequent report.

References

- Avrett, E. H., Fontenla, J. M., & Loeser, R. 1994, Formation of the solar 10830 Å line, in *Infrared Solar Physics*, IAU Symp. No. 154, eds. D. M. Rabin, J. T. Jefferies, & C. Lindsy, Kluwer, Dordrecht, 35.
- Avrett, E. H., & Loeser, R. 2008, Models of the solar chromosphere and transition region from SUMER and HRTS observations: Formation of the extreme-ultraviolet spectrum of hydrogen, carbon, and oxygen, *ApJS*, 175, 229.
- Brekke, P. 1993, An ultraviolet spectral atlas of the Sun between 1190-1730 Å *ApJS*, 87, 443.
- Curdt, W., Brekke, P., Feldman, U., Wilhelm, K., Dwivedi, B. N., Schuhle, U., & Lemaire, P. 2001, The SUMER spectral atlas of solar-disk features, *A&A*, 375, 591.
- Fontenla, J. M., Avrett, E. H., & Loeser, R. 1990, Energy balance in the solar transition region. I. Hydrostatic thermal models with ambipolar diffusion, *ApJ*, 355, 700.
- Fontenla, J. M., Avrett, E. H., & Loeser, R. 1991, Energy balance in the solar transition region. II. Effects of pressure and energy input on hydrostatic models, *ApJ*, 377, 712
- Fontenla, J. M., Avrett, E. H., & Loeser, R. 1993, Energy balance in the solar transition region. III. Helium emission in hydrostatic constant-abundance models with diffusion, *ApJ*, 406, 319.
- Fontenla, J. M., Avrett, E. H., & Loeser, R. 2002, Energy balance in the solar transition region. IV. Hydrogen and helium mass flows with diffusion, *ApJ*, 572, 636.
- Fontenla, J. M., Avrett, E., Thuillier, G., & Harder, J. 2006, Semiempirical models of the solar atmosphere. I. The quiet- and active Sun photosphere at moderate resolution, *ApJ*, 639, 441.
- Fontenla, J. M., Harder, J., Livingston, W., Snow, M., & Woods, R. 2012, High-resolution solar spectral irradiance from extreme ultraviolet to far infrared, *J. Geophys. Res.*, 116, D20108
- Judge, P. G., Carlsson, M., & Stein, R. F. 2003, On the origin of the basal emission from stellar atmospheres : Analysis of solar C II lines, *ApJ*, 597, 1158.
- Linsky, J. L., Bushinsky, R., Ayres, T., Fontenla, J., & France, K. 2012, Far-ultraviolet continuum emission: Applying this diagnostic to the chromospheres of solar-mass stars, *ApJ*, 745, 25L.
- Lites, B. W., Shine, R. A., & Chipman, E. G. 1978, Line formation in the solar chromosphere. I. The C II resonance lines observed with OSO 8, *ApJ*, 222, 333.

Vernazza, J. E., Avrett, E. H., & Loeser, R. 1973, Structure of the solar chromosphere. I. Basic computations and summary of the results, *ApJ*, 184, 605.

Vernazza, J. E., Avrett, E. H., & Loeser, R. 1981, Structure of the chromosphere. III. Models of the EUV brightness components of the quiet Sun, *ApJS*, 45, 635.

Wikstol, O., Hansteen, V. H., Carlsson, M., & Judge, P. G. 2000, Chromospheric and transition region internetwork oscillations: A signature of upward-propagating waves, *ApJ*, 531, 1150.

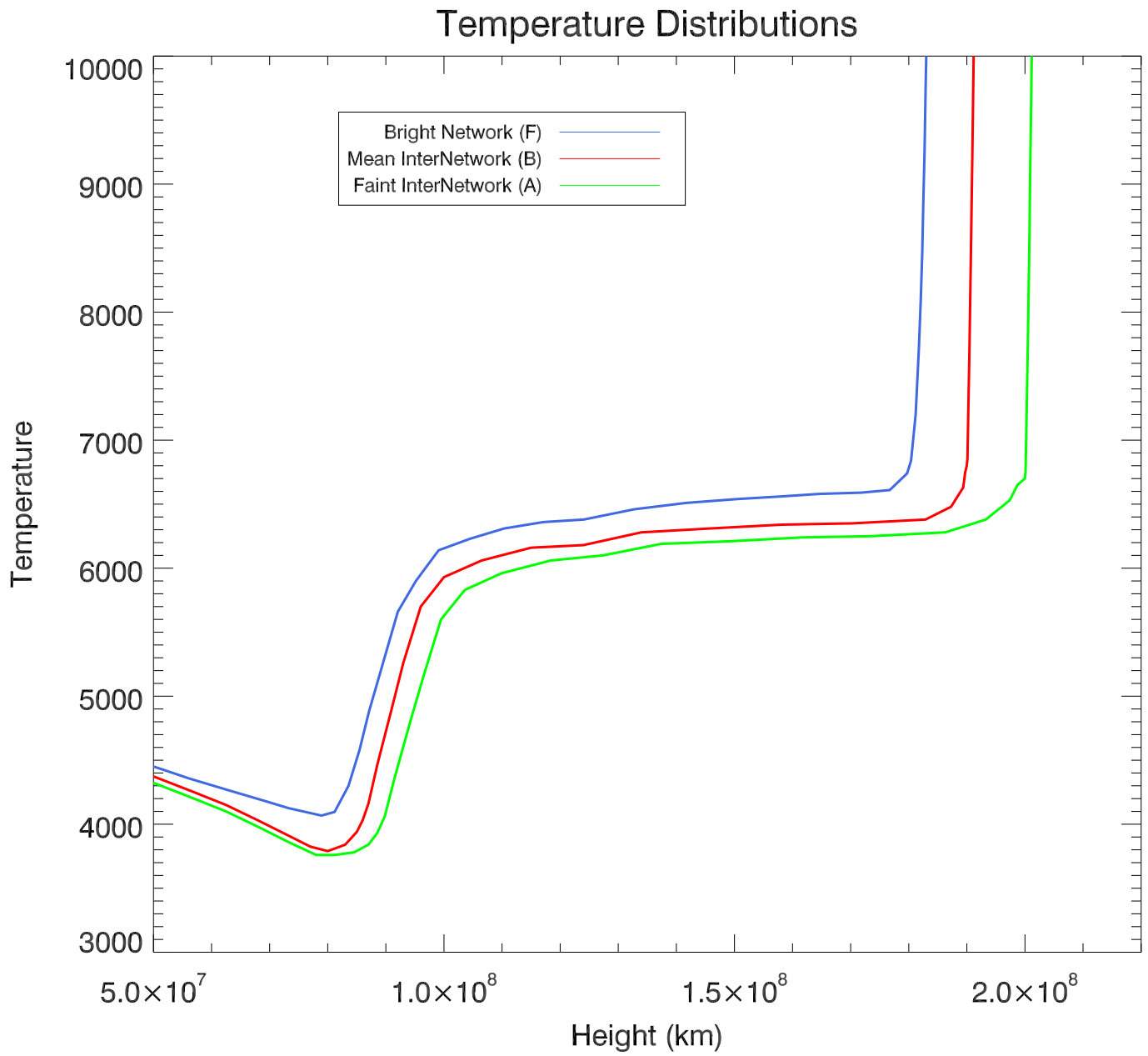


Fig. 1.— Temperature distributions for models A, B, and F.

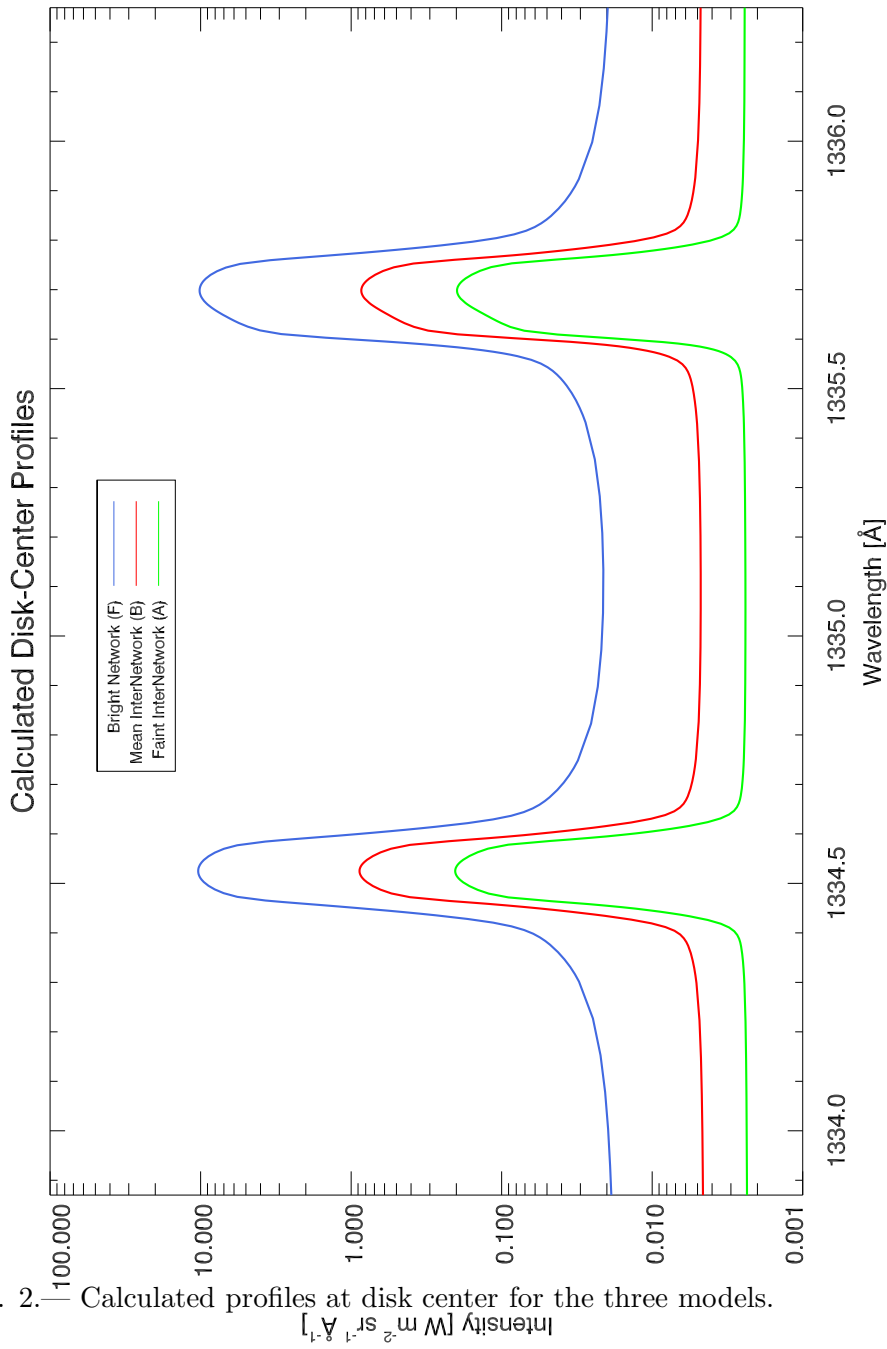


Fig. 2. — Calculated profiles at disk center for the three models.

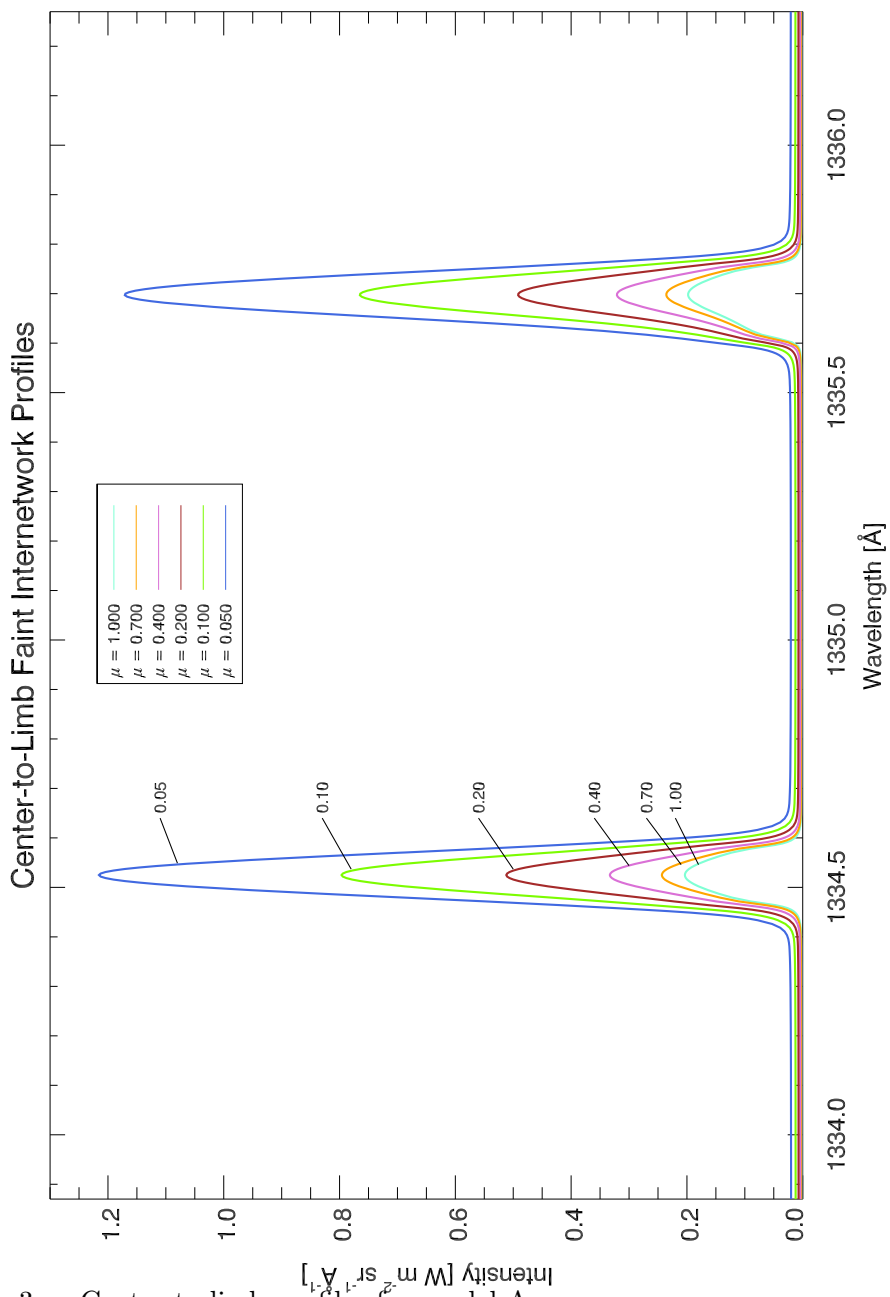


Fig. 3.— Center-to-limb profiles for model A.

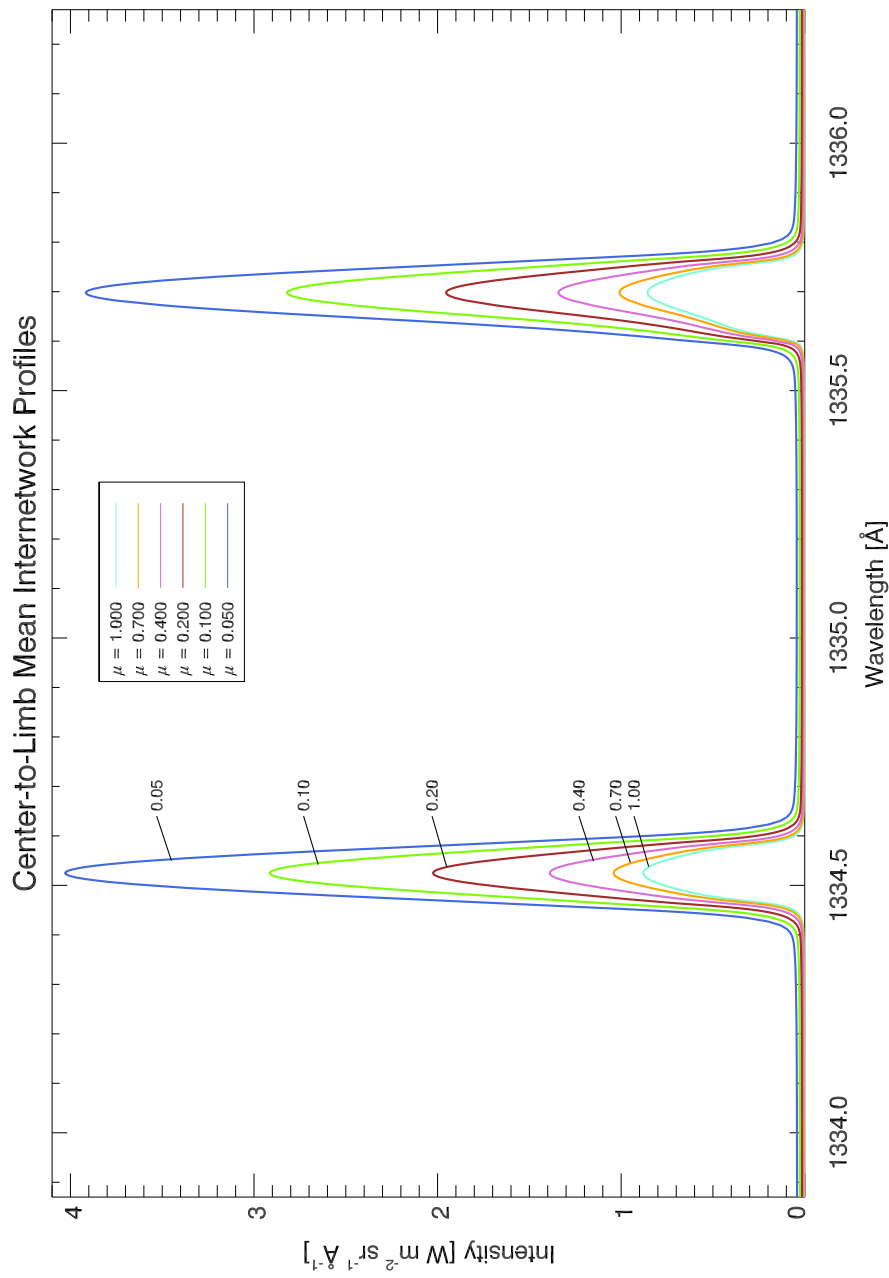


Fig. 4.— Center-to-limb profiles for model C.

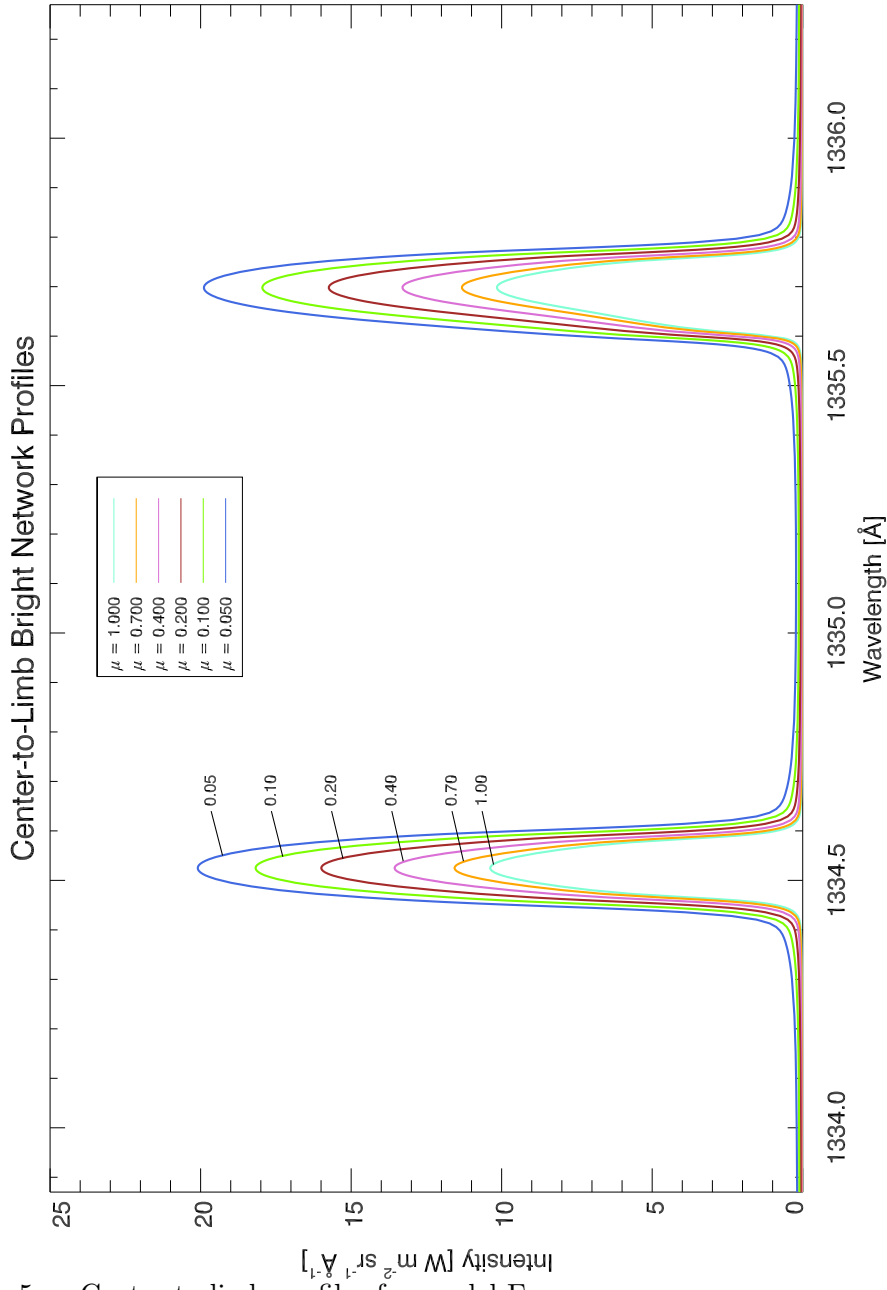


Fig. 5.— Center-to-limb profiles for model F.

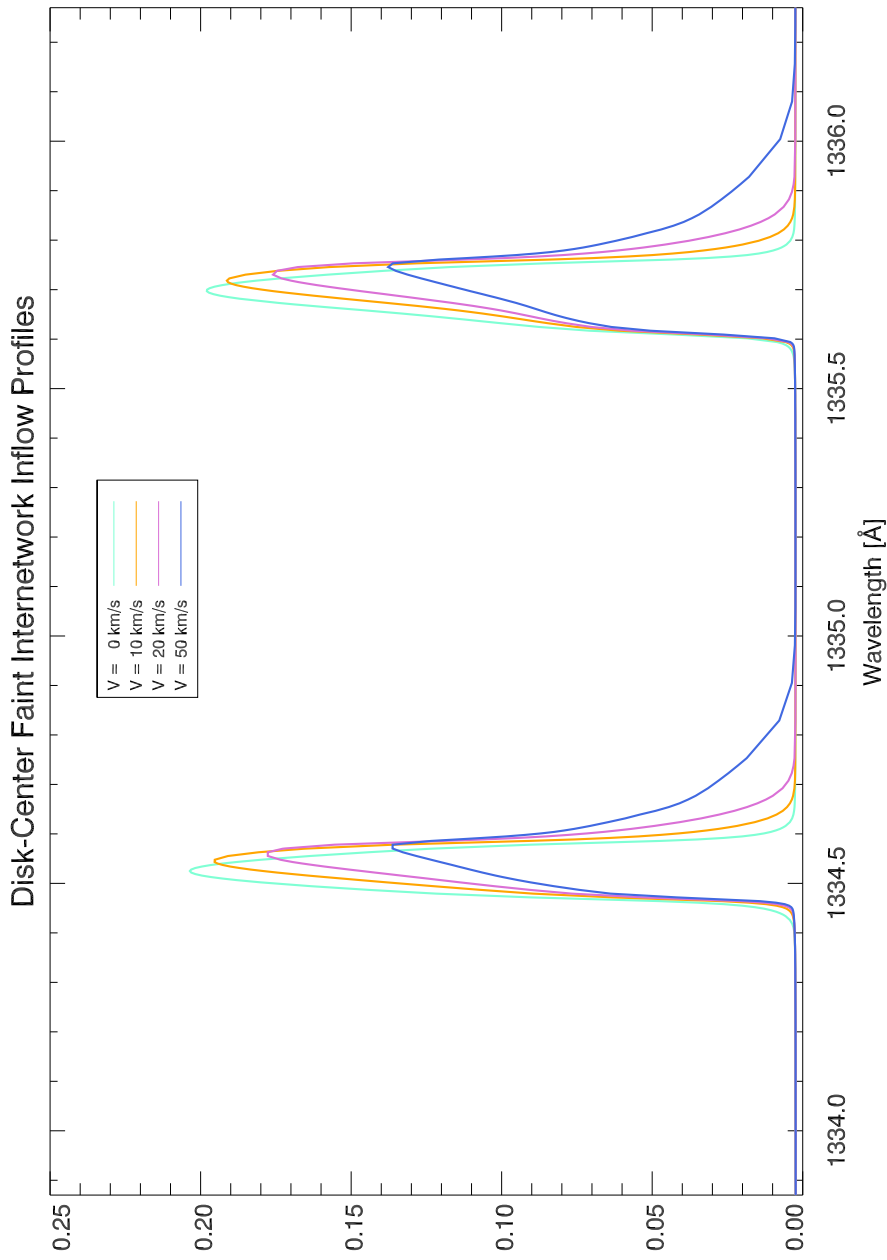


Fig. 6.— Disk-center profiles for model A with inflows.

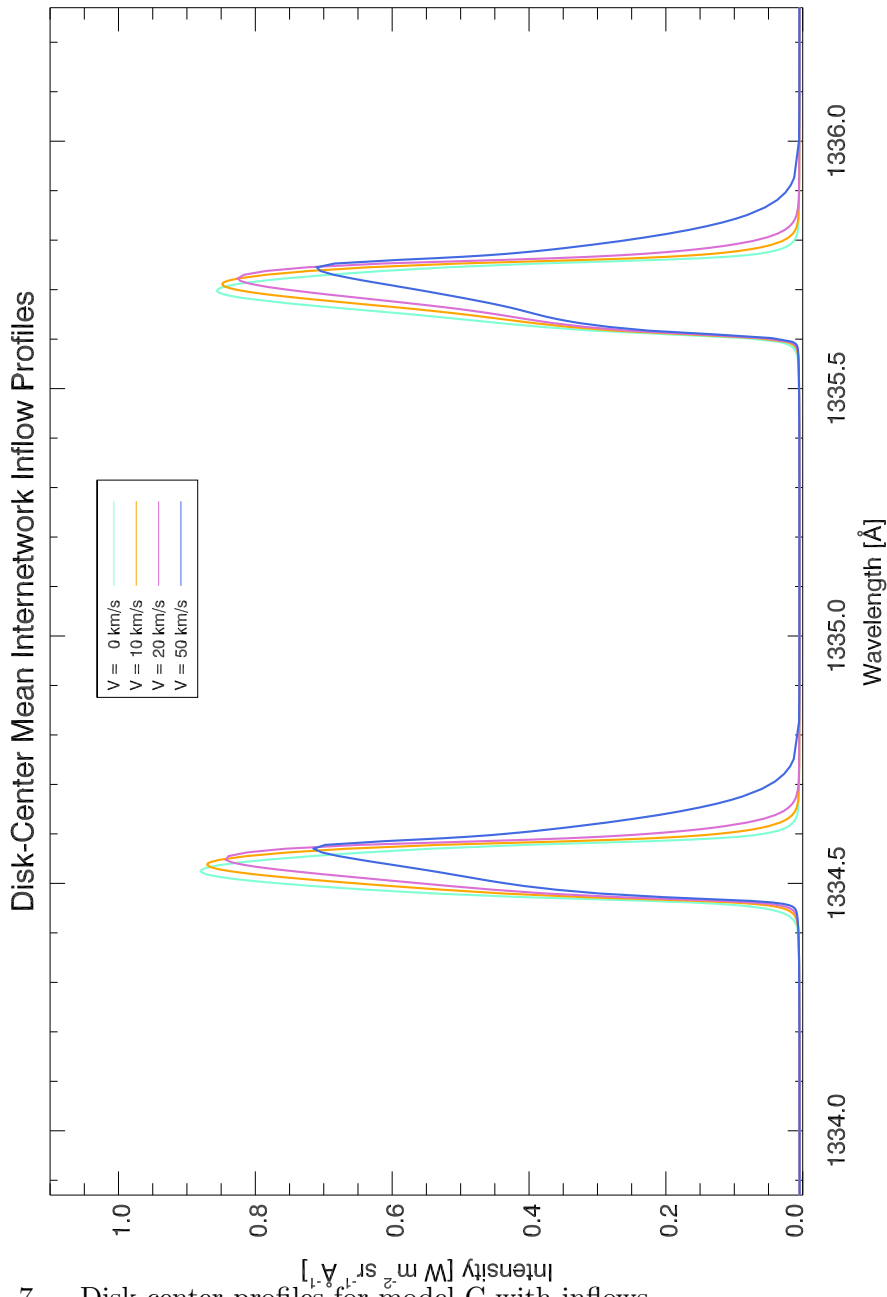


Fig. 7.— Disk-center profiles for model C with inflows.

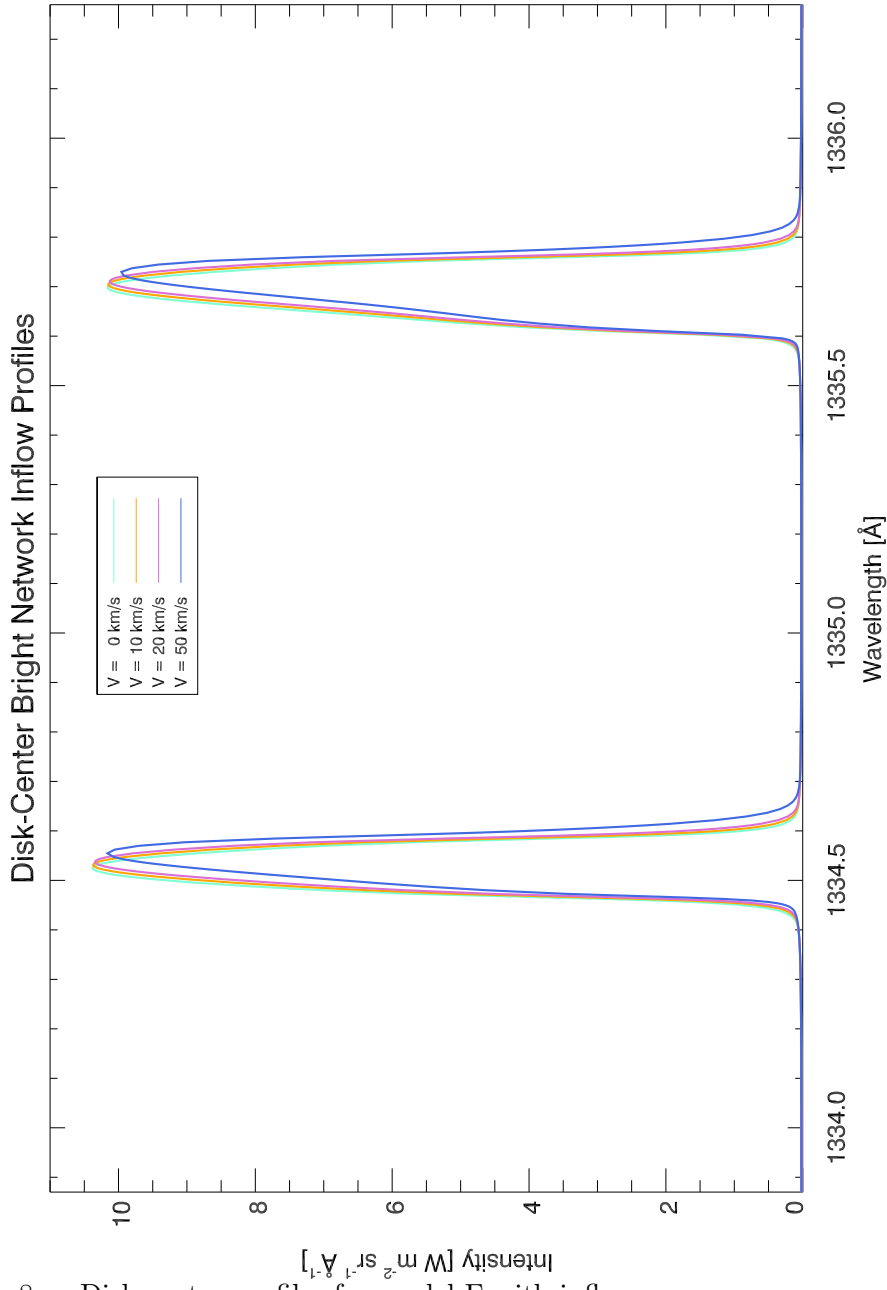


Fig. 8.— Disk-center profiles for model F with inflows.

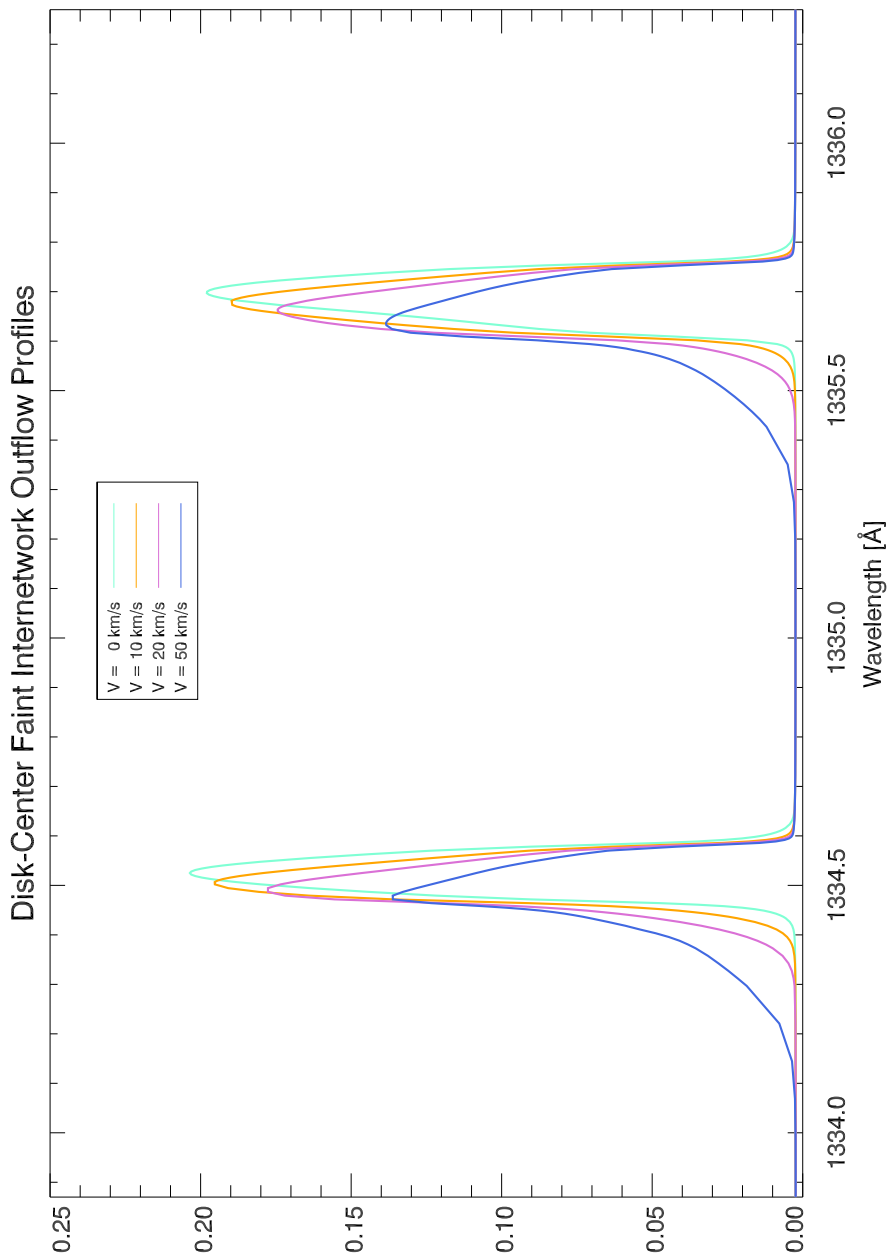


Fig. 9.— Disk-center profiles for model A with outflows.

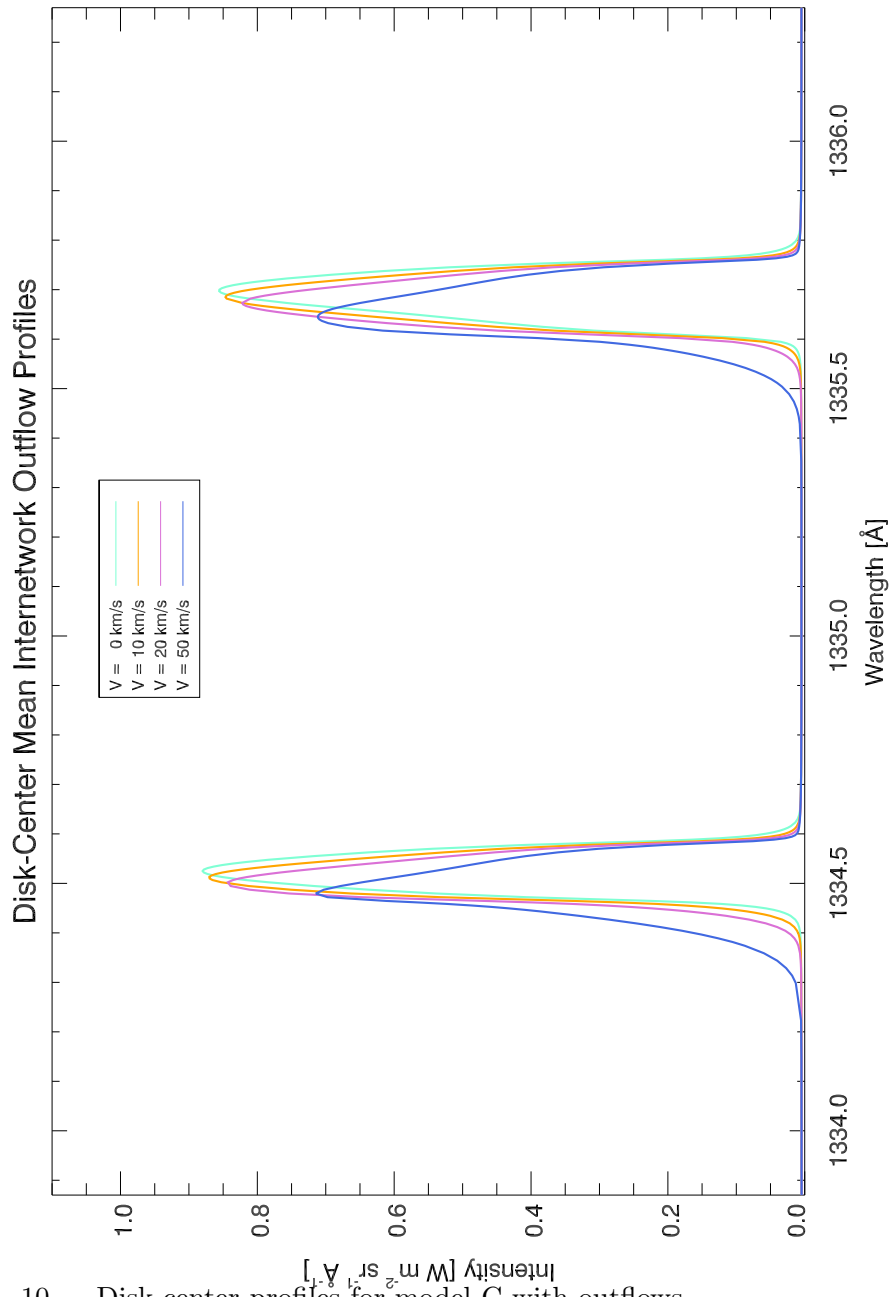


Fig. 10.— Disk-center profiles for model C with outflows.

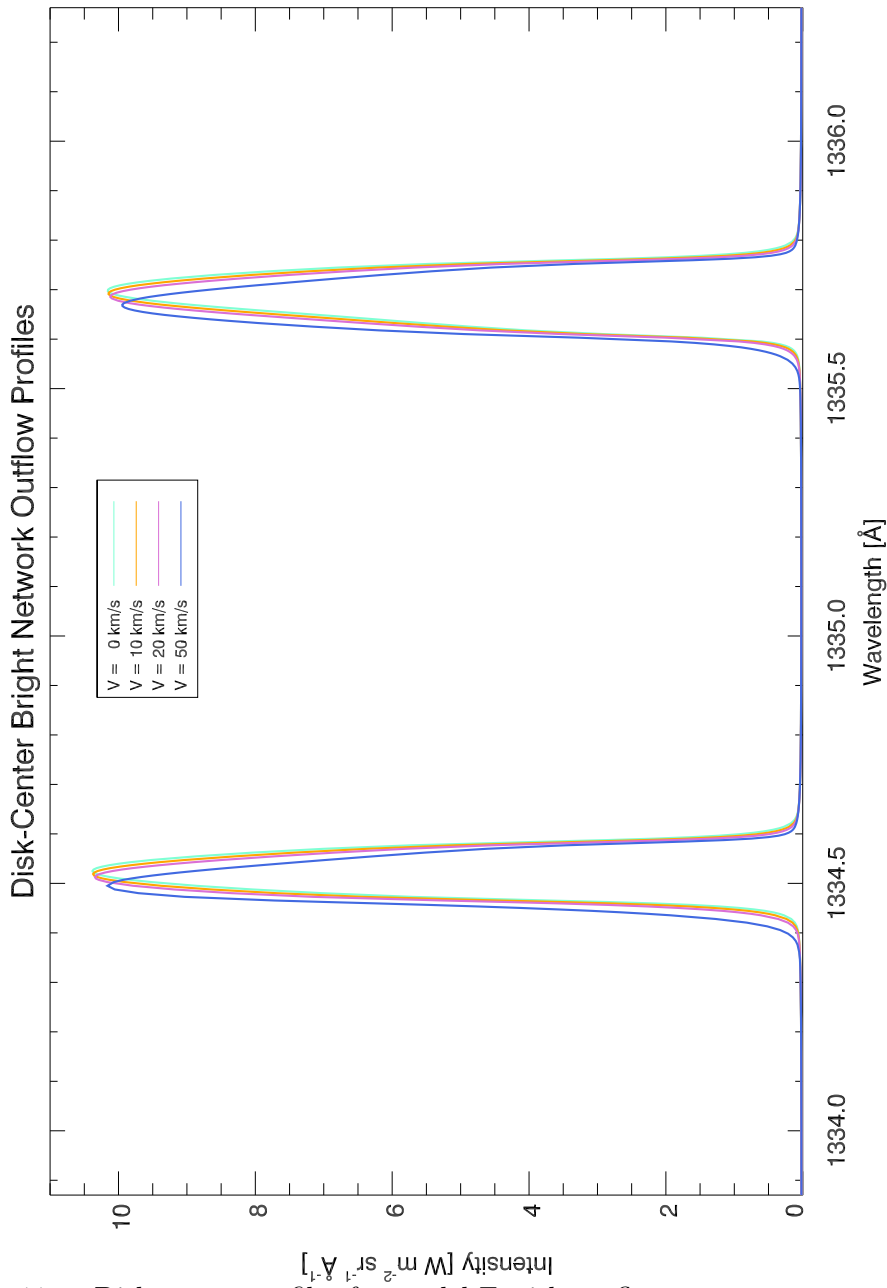


Fig. 11.— Disk-center profiles for model F with outflows.

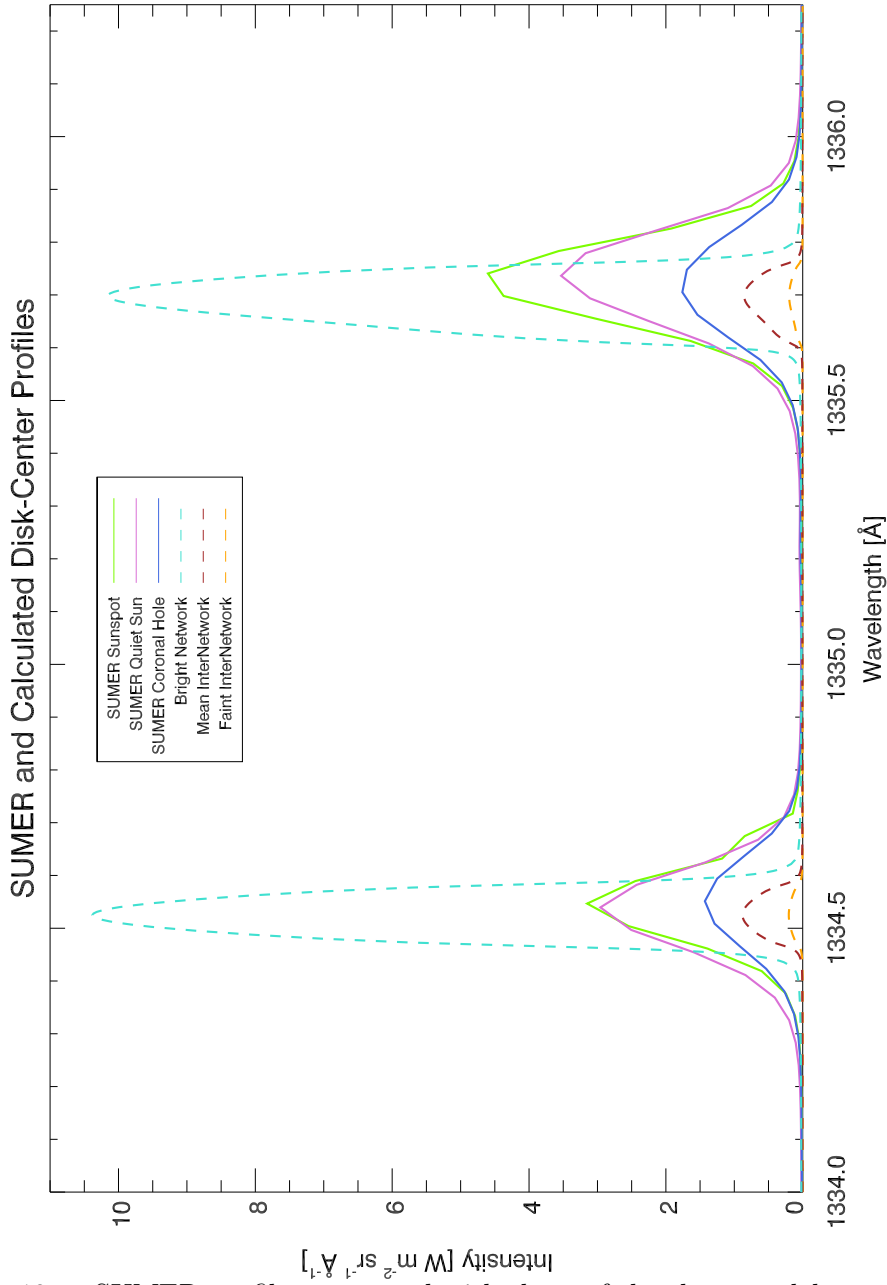


Fig. 12.— SUMER profiles compared with those of the three models.

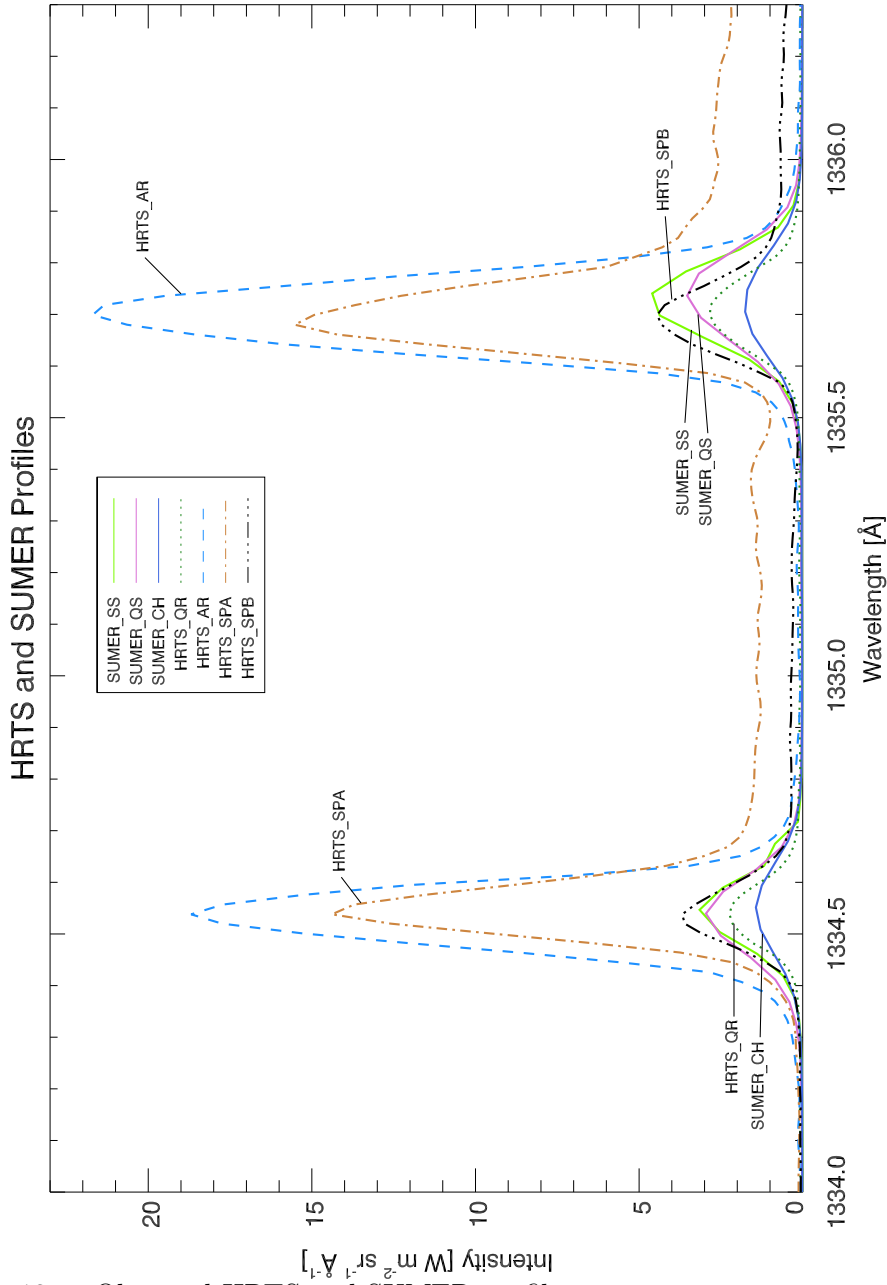


Fig. 13.— Observed HRTS and SUMER profiles.

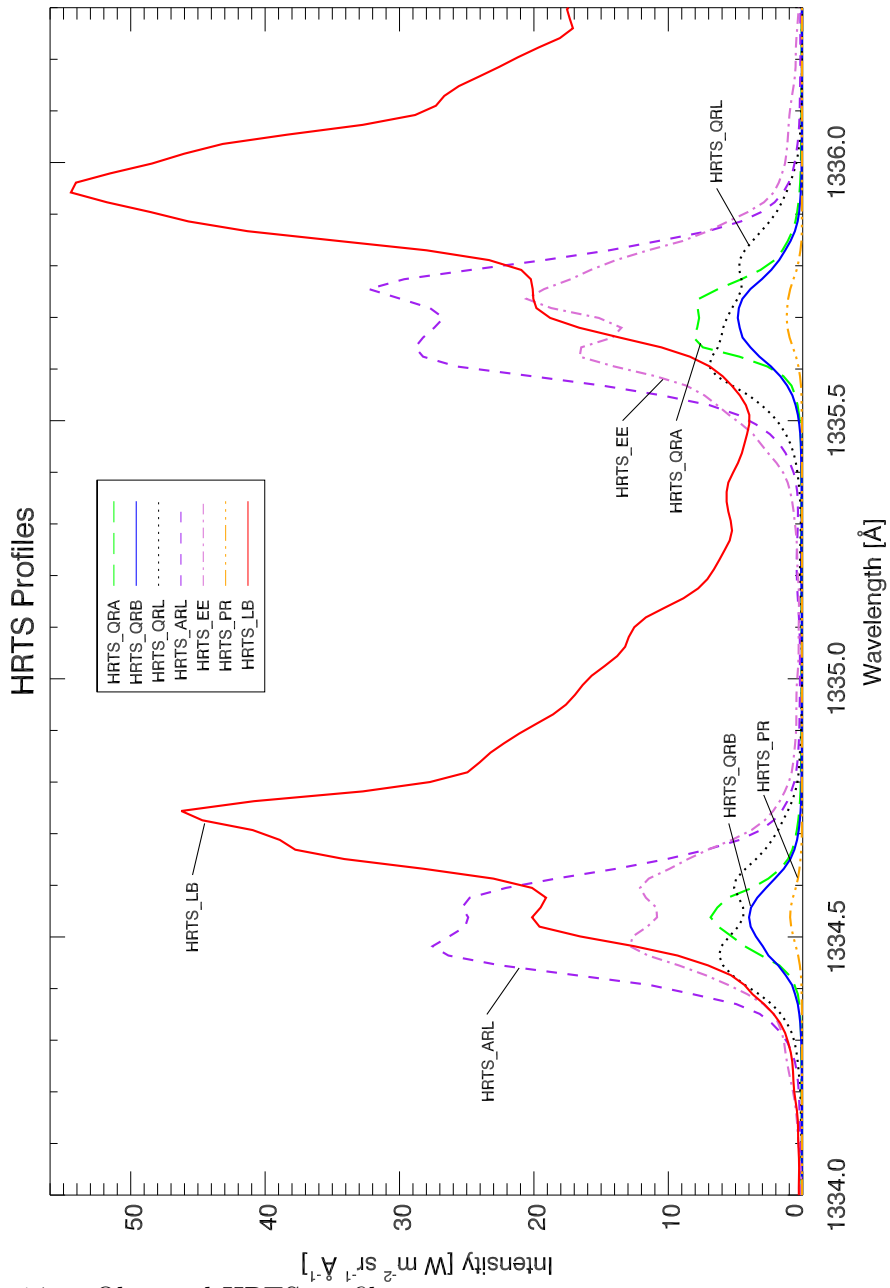


Fig. 14.— Observed HRTS profiles.